

Article

# Titanium Carbide Composite Hollow Cobalt Sulfide Heterojunction with Function of Promoting Electron Migration for Efficiency Photo-Assisted Electro-Fenton Cathode

Fengjiang Chen , Fan Yang <sup>\*</sup>, Sai Che, Hongchen Liu, Neng Chen, Zhijie Wu  and Yongfeng Li <sup>\*</sup>

State Key Laboratory of Heavy Oil Processing, China University of Petroleum, Beijing 102249, China

<sup>\*</sup> Correspondence: yangfan@cup.edu.cn (F.Y.); yfli@cup.edu.cn (Y.L.)

**Abstract:** Constructing heterostructure within electrocatalysts proves to be an attractive approach to adjust the interfacial charge redistribution to promote the adsorption of reactive species and accelerate the charge transfer. Herein, we present the one-pot solvothermal synthesis of Ti<sub>3</sub>C<sub>2</sub> supported hollow CoS<sub>2</sub>/CoS microsphere heterostructure with uneven charge distribution as the cathodic catalyst, which displays a superior quasi-first-order degradation rate (0.031 min<sup>-1</sup>) for sulfamethazine (SMT) in photo-assisted electric-Fenton (EF) process. CoS<sub>2</sub>/CoS/Ti<sub>3</sub>C<sub>2</sub> is proven to favor the 2e<sup>-</sup> oxygen reduction reaction (ORR), with H<sub>2</sub>O<sub>2</sub> selectivity up to 76%. The built-in potential present in the heterojunction helps to accelerate electron transfer, thus promoting the production of H<sub>2</sub>O<sub>2</sub>. Subsequently, H<sub>2</sub>O<sub>2</sub> is rapidly activated to produce ·OH due to the synergistic effect of Co and S. Notably, CoS<sub>2</sub>/CoS/Ti<sub>3</sub>C<sub>2</sub> exhibits enhanced photo-assisted EF (PEF) performance under light. The excellent photocatalysis properties of CoS<sub>2</sub>/CoS/Ti<sub>3</sub>C<sub>2</sub> are attributed to that the unique hollow microsphere structure of catalyst improves the light absorption, and the uneven charge distribution of CoS<sub>2</sub>/CoS heterojunctions promotes the separation of photo-generated holes and electrons. Given the above advantages, CoS<sub>2</sub>/CoS/Ti<sub>3</sub>C<sub>2</sub> cathode delivers a high degradation rate of 98.5%, 91.8%, and 94.5% for SMT, bisphenol A, and sulfadiazine, respectively, with TOC removal efficiency of 76% for SMT with 120 min. This work provides a novel light of the design and construction of efficient PEF cathodes for the treatment of antibiotic wastewater.

**Keywords:** heterojunction; electric-Fenton process; photocatalytic; micro-pollutants



**Citation:** Chen, F.; Yang, F.; Che, S.; Liu, H.; Chen, N.; Wu, Z.; Li, Y. Titanium Carbide Composite Hollow Cobalt Sulfide Heterojunction with Function of Promoting Electron Migration for Efficiency Photo-Assisted Electro-Fenton Cathode. *Catalysts* **2023**, *13*, 253. <https://doi.org/10.3390/catal13020253>

Academic Editor: Enric Brillas

Received: 30 November 2022

Revised: 14 January 2023

Accepted: 20 January 2023

Published: 22 January 2023



**Copyright:** © 2023 by the authors. Licensee MDPI, Basel, Switzerland. This article is an open access article distributed under the terms and conditions of the Creative Commons Attribution (CC BY) license (<https://creativecommons.org/licenses/by/4.0/>).

## 1. Introduction

The environmental problems caused by antibiotics and organic pollutants have become more serious with the progress of human activities, however, conventional water treatment methods are difficult to achieve effective removal of such pollutants [1]. As a kind of electrochemical advanced oxidation processes (EAOPs), Electro-Fenton (EF) is a prospective water pollution treatment method [2] that generate H<sub>2</sub>O<sub>2</sub> through the 2e<sup>-</sup>-ORR by in-situ reduce O<sub>2</sub> at the cathode [3], and then the ·OH can be produced by catalysis of H<sub>2</sub>O<sub>2</sub>. However, the rapid formation of ·OH is usually limited by the yield, selectivity, and reactivation of H<sub>2</sub>O<sub>2</sub> [4]. Therefore, the rapid generation and activation of H<sub>2</sub>O<sub>2</sub> is the key technology for efficient EF reaction [5]. Iron-based catalysis, including FeS, FeS<sub>2</sub>, etc., have been proven to have EF properties for activating H<sub>2</sub>O<sub>2</sub>, however, the tepid H<sub>2</sub>O<sub>2</sub> yield greatly hinder the efficacy of EF technology [6]. One of the common solutions is combination metal-based materials with carbonaceous carriers because of that the oxyfunctional groups and defect sites of the carbon materials provide sufficient approach for the 2e<sup>-</sup> ORR [7–10]. However, the large overpotential and long-term operation of the metal-carbon carrier cathode may cause the metal particles to fall off and carbonaceous carrier poisoning. Additionally, atomic precision doping or defect modulation of carbonaceous carriers may require higher costs. Therefore, it is necessary to find a suitable bifunctional catalyst with efficient 2e<sup>-</sup> ORR selectivity and Fenton performance [11–14].

Cobalt sulfide has a variety of chemical formulas (such as  $\text{CoS}_2$ ,  $\text{CoS}$ ,  $\text{Co}_9\text{S}_8$ ,  $\text{Co}_4\text{S}_3$ ), which have emerged as low-cost and abundant content materials with excellent catalytic activity based on both computational and experimental studies [15–18]. Among them, the metal cobalt pyrite ( $\text{CoS}_2$ ) exhibits excellent  $2e^-$  ORR activity to produce  $\text{H}_2\text{O}_2$  due to the single porphyrin structure of  $\text{CoS}_2$  inhibiting the O–O bond breaking of and promoting the production of  $\text{H}_2\text{O}_2$ , and the high  $2e^-$  ORR selectivity of  $\text{CoS}_2$  is expected to serve as a high efficiency catalyst in EF reaction [16]. Additionally, hexagonal cobalt sulfide ( $\text{CoS}$ ) is commonly used in Fenton-like fields because of narrow band gap structure and efficient activation of  $\text{H}_2\text{O}_2$  performance, which is attributed to that  $\text{CoS}$  can provide suitable Lewis acid strength to adsorb and catalyze  $\text{H}_2\text{O}_2$  to produce  $\cdot\text{OH}$  [17]. Besides, the synergistic effect of Co and S effectively promotes electron transfer and accelerates the recycling of cobalt active species [18,19]. It is well known that cobalt sulfide with different formulas can interact with each other to form heterojunction with two opposite charge space field and built-in electric field area [20–22], which will promote the formation of uneven charge distribution. This uneven charge distribution may be able to facilitate the charge carrier transport in the photo-assisted electric-Fenton (PEF) process, thus exhibiting enhanced photo-assisted electrocatalytic activity [23]. However, the application of cobalt sulfide in electrocatalysis is always limited in its general conductivity. Transition metal carbide (Mxenes), as a novel two-dimensional material, exhibits excellent electrical conductivity (Titanium carbide( $\text{Ti}_3\text{C}_2$ )~9880  $\text{S cm}^{-1}$ ) [24,25] and highly exposed metal sites, which has great potential in the field of photocatalysis and electrochemistry, such as li-ion battery, supercapacitors, and photocatalytic hydrogen production [26–29]. There are reports that Ti metal at the end of titanium carbide exhibits poor oxygen resistance due to the high amount of exposed metal atoms, which promotes the regeneration of active sites [28]. In addition, the Schottky junction formed between  $\text{Ti}_3\text{C}_2$  and metal semiconductors can suppress the photo-generated holes and electrons recombination, which also helps to enhance the photo-assisted EF performance [30–32]. Therefore, the combination of hollow heterostructure  $\text{CoS}_2/\text{CoS}$  with  $\text{Ti}_3\text{C}_2$  is meaningful for maintaining the  $2e^-$  ORR behavior of  $\text{CoS}_2$  and Fenton behavior of  $\text{CoS}$  while optimizing activity, electrical conductivity, and sustainability of  $\text{CoS}_2/\text{CoS}$ .

In this work, heterojunction  $\text{CoS}_2/\text{CoS}$  nanocomposites with  $\text{Ti}_3\text{C}_2$  were prepared by simple hydrothermal synthesis.  $\text{CoS}_2/\text{CoS}/\text{Ti}_3\text{C}_2$  cathode displayed a superior degradation performance for sulfamethazine (SMT) with degradation rates of  $0.031 \text{ min}^{-1}$ . Rotating disk electrode (RDE) tests exhibit that  $\text{CoS}_2/\text{CoS}/\text{Ti}_3\text{C}_2$  has excellent  $2e^-$  ORR characteristics, which contributes to promote the rapid production of  $\text{H}_2\text{O}_2$ . In addition, the uneven charge distribution accelerates the migration of charge carriers to facilitate photo-assisted EF process. UV-Vis DRS proves that  $\text{CoS}_2/\text{CoS}/\text{Ti}_3\text{C}_2$  has strong light absorption in the visible and UV regions, and the PL spectrum demonstrates that  $\text{CoS}_2/\text{CoS}/\text{Ti}_3\text{C}_2$  is provided with excellent charge-hole separation efficiency, which is attributed to the excellent electron-withdrawing characteristics of  $\text{Ti}_3\text{C}_2$ , as well as the heterostructure in  $\text{CoS}_2/\text{CoS}$ . The total organic carbon (TOC) removal rate of SMT within 120 min is as high as 76%, and the possible degradation pathways of SMT are given based on UPLC-M-QTOF. The above work indicates that  $\text{CoS}_2/\text{CoS}/\text{Ti}_3\text{C}_2$  as a novel electrode material enriches the choice of available cathode materials and offers a new way for the degradation of persistent pollutants in the PEF process.

## 2. Results

The synthesis of  $\text{CoS}_2/\text{CoS}/\text{Ti}_3\text{C}_2$  involved of  $\text{CoS}_2/\text{CoS}$  and subsequent  $\text{CoS}_2/\text{CoS}/\text{Ti}_3\text{C}_2$  (Figure 1). The prepared  $\text{Ti}_3\text{C}_2$  was distributed in tetramethylammonium hydroxide (TMAOH) solution and processed with ultrasonic waves, and the exfoliated  $\text{Ti}_3\text{C}_2$  was added to the solvothermal process of  $\text{CoS}_2/\text{CoS}/\text{Ti}_3\text{C}_2$ . Finally, hollow  $\text{CoS}_2/\text{CoS}$  grown in situ on the surface of  $\text{Ti}_3\text{C}_2$ . For comparison, the  $\text{CoS}_2$ ,  $\text{CoS}_2/\text{CoS}$ , and  $\text{CoS}$  were obtained under the conditions of  $V_{\text{EG}}:V_{\text{DMF}} = 0.5, 0.9, \text{ and } 2$ , respectively.

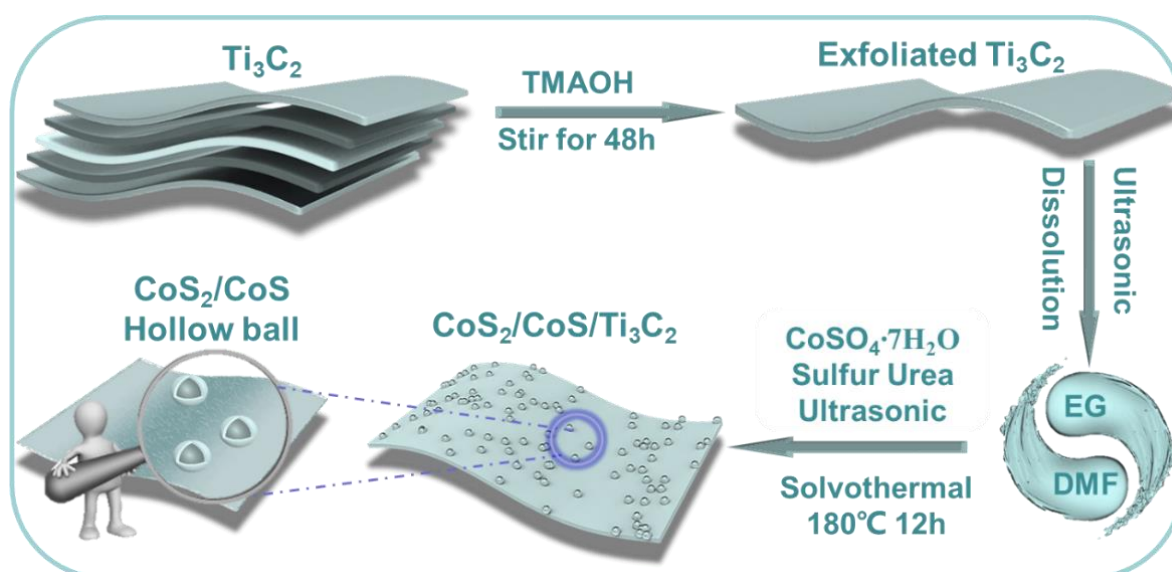


**Figure 1.** Schematic illustration for the composition of  $\text{CoS}_2/\text{CoS}/\text{Ti}_3\text{C}_2$ .

As shown in Figure 2a, all characteristic peaks could be well attributed to the diffraction peaks of CoS (PDF#65-3418) and  $\text{CoS}_2$  (PDF#89-1492) [33] while  $V_{\text{DMF}}:V_{\text{EG}} = 0.5$  and 2. The mixed phase of  $\text{CoS}_2$  and CoS is obtained when the value of  $V_{\text{EG}}:V_{\text{DMF}}$  is 0.9 [22,34]. The characteristic peaks of  $\text{Ti}_3\text{C}_2$  ( $36.4^\circ$ ) can be found in  $\text{CoS}_2/\text{CoS}/\text{Ti}_3\text{C}_2$ . As shown in Raman spectra (Figure 2b), the peaks at  $\sim 293\text{ cm}^{-1}$  ( $E_g$ ), and  $\sim 393\text{ cm}^{-1}$  ( $A_g$ ) match well with the value of  $\text{CoS}_2$  in reference [22,35]. The peaks at  $\sim 475$ , and  $\sim 670\text{ cm}^{-1}$  represent the  $E_g$ , and  $A_{1g}$  pattern of CoS [36], respectively. Both the characteristic peaks of  $\text{CoS}_2$  ( $\sim 392.5\text{ cm}^{-1}$ ) and CoS ( $\sim 476.0$  and  $679.0\text{ cm}^{-1}$ ) can be discovered in the pattern of  $\text{CoS}_2/\text{CoS}/\text{Ti}_3\text{C}_2$ . It is worth noting that the peaks corresponding of  $\text{CoS}_2$  and CoS are red-shifted and blue-shifted in heterojunction, respectively. The opposite shifts of CoS and  $\text{CoS}_2$  characteristic peaks in Raman indicates the creation of a built-in potential region due to the production of heterojunctions, which help to promote electrons transport and enhance catalytic performance.

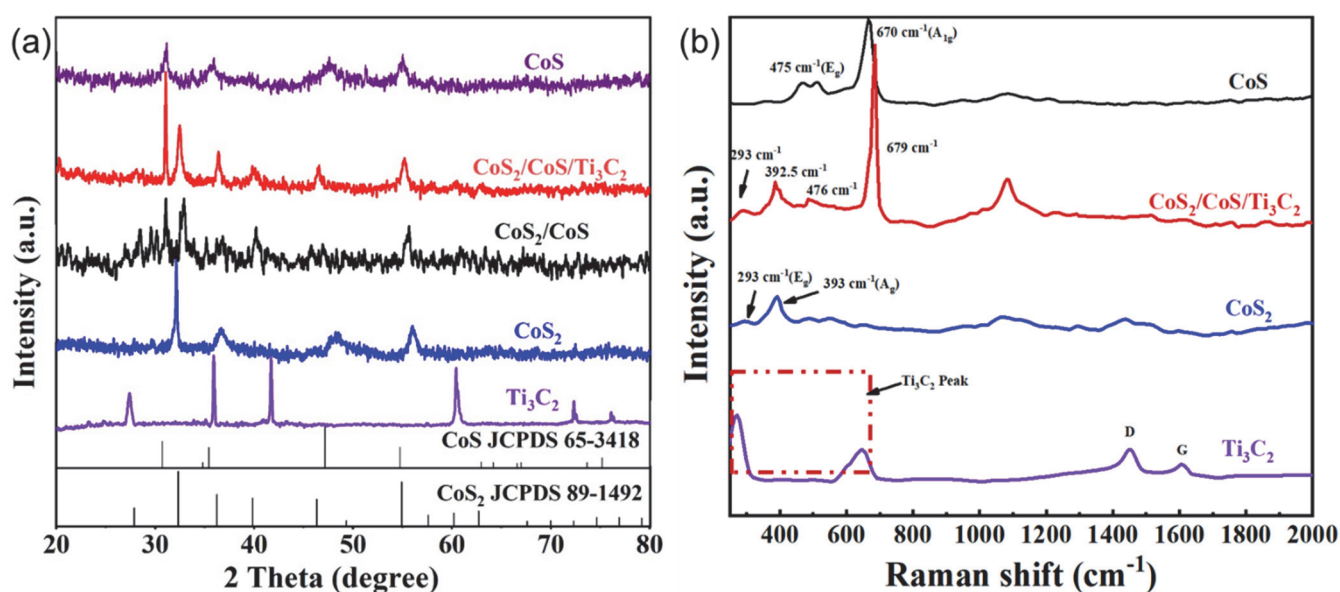


**Figure 2.** (a) X-ray powder diffraction (XRD) and (b) Raman characterization.

The morphology of  $\text{Ti}_3\text{C}_2$  before HF etching shows a multi-layered bulk structure (Figure S1). SEM images of exfoliated  $\text{Ti}_3\text{C}_2$  and  $\text{CoS}_2/\text{CoS}/\text{Ti}_3\text{C}_2$  are detected in Figure 3. The  $\text{Ti}_3\text{C}_2$  peeled off by the intercalation method showed a uniform monolithic structure with slight wrinkles on the surface. With  $\text{CoS}_2/\text{CoS}$  compounded with  $\text{Ti}_3\text{C}_2$ ,  $\text{CoS}_2/\text{CoS}$  is evenly dispersed on the surface of  $\text{Ti}_3\text{C}_2$  (Figure 3b,c), which is due to the excellent dispersing effect of lot of terminating groups on  $\text{Ti}_3\text{C}_2$  surface. More interestingly, the particles on the surface of  $\text{Ti}_3\text{C}_2$  show typical hollow characteristics at high magnification (Figure 3d). The TEM of the  $\text{CoS}/\text{CoS}_2$  heterostructure showed the characteristics of hollow microspheres (Figure 4a), and the diameter of the microspheres is about 50 nm, and the particle size is relatively uniform. The wrinkled  $\text{Ti}_3\text{C}_2$  lamella can be seen in Figure 4b,c, which demonstrated that the successfully combination of  $\text{CoS}/\text{CoS}_2$  and  $\text{Ti}_3\text{C}_2$ . Plain stripe spacing of 0.248 nm, 0.279 nm can be observed in the high-resolution TEM picture (Figure 4d), which corresponds to the plane (200) and (210) of  $\text{CoS}_2$ , and interplanar spacing of 0.193 nm and 0.252 nm can be assigned to the plane (102) and (101) of  $\text{CoS}$  [22,33]. The clear lattice stripes and the absence of obvious amorphous regions at the interface between  $\text{CoS}_2$  and  $\text{CoS}$  confirm the formation of heterojunctions (Figure 4e). The overlapping patterns of diffraction rings of  $\text{CoS}_2/\text{CoS}$  indicated both the formation of heterostructure and its good crystallinity (Figure 4f). Therefore, the heterogeneous structure of  $\text{CoS}_2/\text{CoS}$  was successfully prepared. The element mappings of TEM and SEM demonstrates that Co and S mainly exist on the microspheres, and S and Co are uniformly distributed on the  $\text{Ti}_3\text{C}_2$  surface, indicating that cobalt sulfide and  $\text{Ti}_3\text{C}_2$  form a good composite structure (Figure 4g).

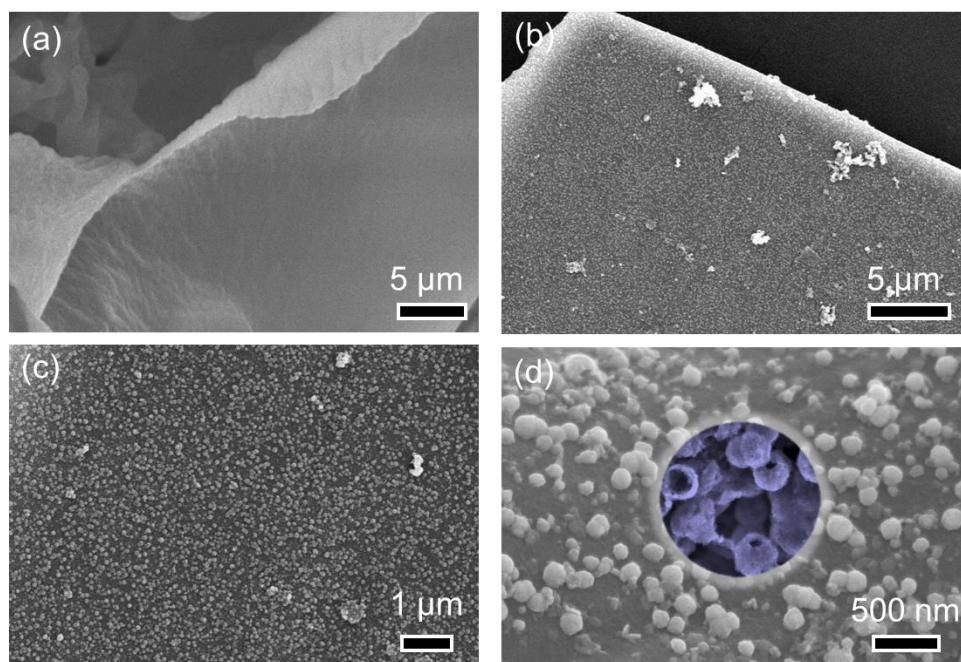


**Figure 3.** SEM images of (a)  $\text{Ti}_3\text{C}_2$ , (b–d)  $\text{CoS}_2/\text{CoS}/\text{Ti}_3\text{C}_2$  under different magnifications.

Without the addition of  $\text{Ti}_3\text{C}_2$ ,  $\text{CoS}_2/\text{CoS}$  exhibits the characteristics of aggregated particles (Figure S2a). Interestingly, the addition of  $\text{Ti}_3\text{C}_2$  can form uniformly dispersed hollow microspheres. This difference [37] may be caused by the following reasons. Firstly, the functional group of  $\text{Ti}_3\text{C}_2$  have a clear tendency to coordinate with  $\text{Co}^{2+}$  ions to generate the stable chelate complexes. The effect of  $\text{Ti}_3\text{C}_2$  is commanding the release speed of  $\text{Co}^{2+}$  via the coordinating effect of  $\text{Ti}_3\text{C}_2\text{-Co}^{2+}$  chelate composite, thus slowing down deposition rate of  $\text{CoS}_2$  and  $\text{CoS}$  to facilitate the regulation of  $\text{CoS}_2/\text{CoS}$  hollow microparticles. In the initial step, the sulfur powder in solution is converted by the reduction of urea, which contributes to the rapid acquisition of soft-template S-core at ambient temperature. At the same time,  $\text{Co}^{2+}$  is uniformly dispersed on the surface of S-core. As the reaction proceeds,

CoS<sub>2</sub> and CoS with interaction could be generated after crystal growth overcoming the anisotropy, thereby successfully introducing the heterogeneous structure. With the rise of reaction temperature, the S-core fades away, and the internal cavity becomes apparent, resulting in the formation of CoS<sub>2</sub>/CoS hollow microspheres with heterogeneous structure. Some examinations have shown that the hollow structure can exhibit a kinetically good open surface structure and a shorter mass and charge transport diffusion path [37]. Therefore, while this unique structure provides more active sites, the shorter mass and charge diffusion paths accelerate the ORR process of H<sub>2</sub>O<sub>2</sub> synthesis and the subsequent Fenton process, thereby effectively improving the degradation efficiency. In addition, the multiple reflection of light in the hollow structure can also improve the efficiency of light utilization, which may improve the light absorption performance, thereby enhancing the PEF process.

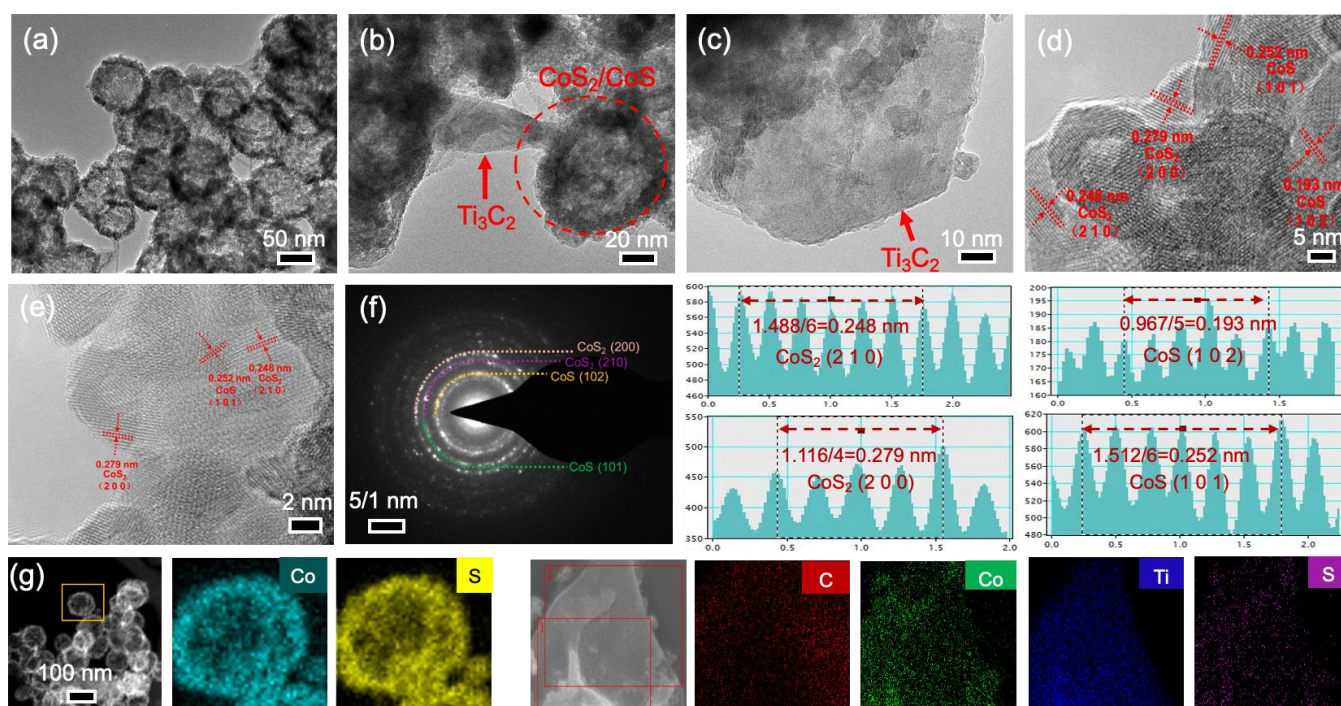


**Figure 4.** (a–e) CoS<sub>2</sub>/CoS/Ti<sub>3</sub>C<sub>2</sub> HRTEM images. (f) Different lattice fringes correspond to diffraction rings patterns (g) corresponding EDS elemental mapping of C, Co, Ti, and S.

The corresponding characteristic peaks of S 2p and Co 2p are displayed in CoS, CoS<sub>2</sub>, CoS<sub>2</sub>/CoS, and the peaks of Ti 2p could also be noticed in CoS<sub>2</sub>/CoS/Ti<sub>3</sub>C<sub>2</sub> (Figure 5a). The high-resolution Ti 2p spectrum of CoS<sub>2</sub>/CoS/Ti<sub>3</sub>C<sub>2</sub> exhibits peaks at ~464.8, ~458.5 eV corresponds to Ti-O (Figure 5b), and the peak centered at 472.0 eV could be assigned to Ti-F, indicating the existence of Ti<sub>3</sub>C<sub>2</sub> [28]. For the Co 2p spectrum, two distinct peaks can be found at binding energy of ~779 and 797.5 eV, indicating the presence of Co<sup>2+</sup>, which can be attributed to Co-S [33,34,37,38]. Two correlative characteristic lines at 782.5 and 802.4 eV can be attributed to satellite peaks of Co<sup>2+</sup> and Co<sup>3+</sup> (Figure 5c). In order to gain a clearer comprehending of the formation of CoS<sub>2</sub>/CoS heterojunctions as well as the charge distribution at the interface, S 2p was further investigated. The characterized S<sub>2</sub><sup>2-</sup> peaks at 162.3, 163.5 eV and the S<sup>2-</sup> at 161.5, 162.7 eV can be observed in CoS<sub>2</sub> and CoS, respectively (Figure 5d). It is not difficult to find that the binding energy of S 2p<sub>3/2</sub> (S<sup>2-</sup>) in CoS<sub>2</sub>/CoS structure move mildly to a lower energy about 0.1 eV than that in CoS because of additional negative charges in CoS side, in contrast, the energy of S<sub>2</sub><sup>2-</sup> is marginally higher than that in CoS<sub>2</sub> [39], therefore, the distribution of opposite charges in CoS<sub>2</sub>/CoS and CoS<sub>2</sub>/CoS/Ti<sub>3</sub>C<sub>2</sub> can be determined because of the electrons shift of S 2p<sub>3/2</sub> in the opposite direction.

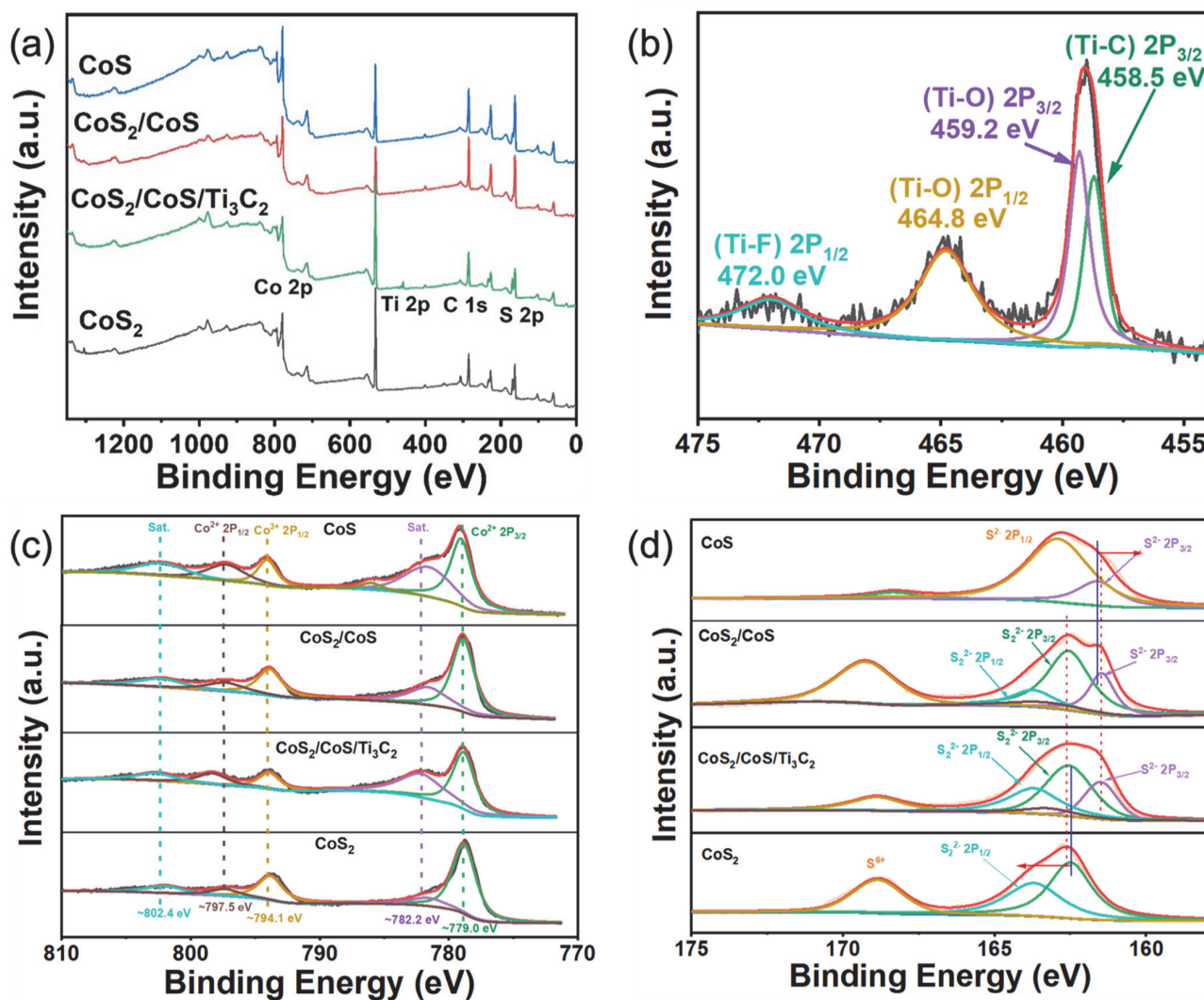


**Figure 5.** (a) XPS survey spectra of  $\text{CoS}_2$ ,  $\text{CoS}$ ,  $\text{CoS}_2/\text{CoS}$ ,  $\text{CoS}_2/\text{CoS}/\text{Ti}_3\text{C}_2$ , and high-resolution XPS spectra (b) Ti 2p of  $\text{CoS}_2/\text{CoS}/\text{Ti}_3\text{C}_2$ . High-resolution (c) Co 2p, (d) S 2p of  $\text{CoS}_2$ ,  $\text{CoS}$ ,  $\text{CoS}_2/\text{CoS}$ , and  $\text{CoS}_2/\text{CoS}/\text{Ti}_3\text{C}_2$ .

The influence of different cobalt sulfide crystal phases and composites on EF property was discussed in Figure 6a. 10 mg/L antibiotic solution in 0.05 mol/L  $\text{Na}_2\text{SO}_4$  was considered as degraded pollutant and different samples loaded on carbon cloth (CC) as the cathodes. Note that  $\text{CoS}_2/\text{CoS}/\text{Ti}_3\text{C}_2$  displays the highest attenuation performance (~67%, 90 min) under the condition of electricity without light, which is higher than that of  $\text{CoS}$  (~45%, 90 min),  $\text{CoS}_2$  (~56%, 90 min), and  $\text{CoS}_2/\text{CoS}$  (~60%, 90 min). This result may be assigned to the excellent synergy between  $\text{CoS}_2$ ,  $\text{CoS}$  and  $\text{Ti}_3\text{C}_2$ , which significantly improves the transfer efficiency of charge carriers in  $2e^-$  ORR, thereby helping to accelerate the formation of  $\cdot\text{OH}$ . pH value generally has a significant impact for PEF systems involving transition metal-based catalyst. The catalytic performance of  $\text{CoS}_2/\text{CoS}/\text{Ti}_3\text{C}_2$  at different pH is shown in Figure 6b. As the initial pH decreases from 9 to 3, the removal performance of SMT improves from 48% to 80.5%.  $\text{CoS}_2/\text{CoS}/\text{Ti}_3\text{C}_2$  at pH = 3, 5, 7, 9 displays completely different attenuation efficiencies for SMT, which is helpful to show new viewpoint of the influence of catalyst on the efficiency of pollutants, as well as the formation of active components.  $\text{CoS}_2/\text{CoS}/\text{Ti}_3\text{C}_2$  shows a well documented prevalence of pH values, with similar attenuation of organic compounds at pH of 5–9. The removal efficiency at pH = 3 is significantly higher than that at other pH conditions due to the lowered oxidation potential of  $\cdot\text{OH}$  at high pH values (2.6–2.8 eV at pH = 3 and 1.90 eV at pH = 7).

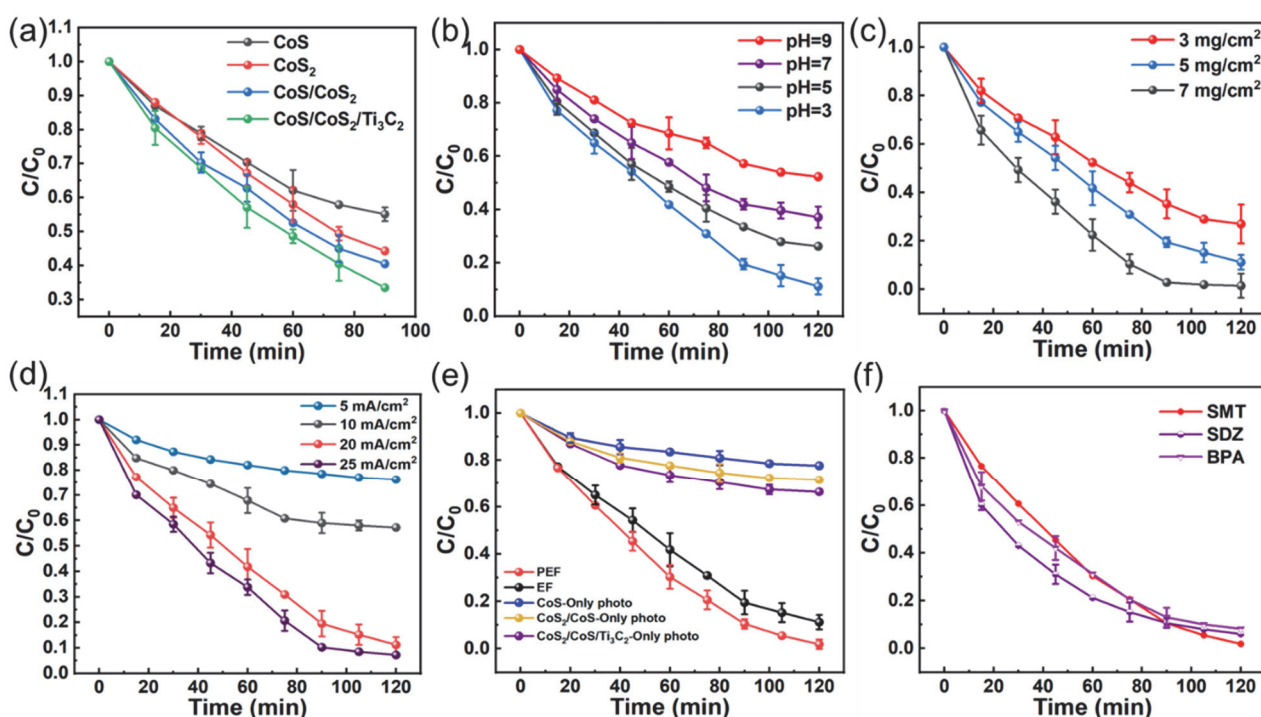


**Figure 6.** Removal efficiency of prepared samples in different reaction systems, (a) CoS<sub>2</sub>, CoS, and CoS<sub>2</sub>/CoS, CoS<sub>2</sub>/CoS/Ti<sub>3</sub>C<sub>2</sub> (pH ≈ 5), (b) different initial pH (c) different catalyst loading (pH ≈ 3), (d) different current intensity, (e) EF under different light conditions, (f) Different reaction substrates. Unless otherwise stated, the reaction conditions are SMT = 10 mg/L, 100 mL; catalyst = 5 mg/cm<sup>2</sup>; I = 20 mA/cm<sup>2</sup>; under electricity without light.

The influence of catalyst load on degradation performance is shown in Figure 6c. With the increase in catalyst dosage from 3 mg/cm<sup>2</sup> to 7 mg/cm<sup>2</sup>, the degradation rate of SMT improved from 73% to 98.4% (under electricity without light, 120 min, SMT = 10 mg/L). An increase in the catalyst loading capacity brings about an increase in the number of active sites, which contributes to improved degradation performance of SMT. The effect of current is investigated in Figure 6d. When the current intensity reaches 20 mA/cm<sup>2</sup>, the EF performance (89%) of the CoS<sub>2</sub>/CoS/Ti<sub>3</sub>C<sub>2</sub> is significantly higher than that of 10 mA/cm<sup>2</sup> (43%) and 5 mA/cm<sup>2</sup> (24%), which is due to that the increase in current can provide more cathode electrons, thereby enhancing the oxygen reduction activity of the material. However, with the further rise of current intensity, the degradation rate of SMT did not show a significant increase, which may be associated with the occurrence of H<sub>2</sub>O<sub>2</sub> decomposition at high currents. The synergistic effect of photo on EF is shown in Figure 6e, compared to the EF process without light, the removal performance of SMT increased by 10% within 120 min, and SMT decay rate can reach 98.5% under PEF conditions, and the reactions rate is as high as 0.031 min<sup>-1</sup> (Figure S4), which is better than that of part reported cathodes (Table S1). Moreover, under the condition of light-only, the removal rate of CoS<sub>2</sub>/CoS/Ti<sub>3</sub>C<sub>2</sub>-cathode can reach 34.5% within 120 min, which is higher than that of CoS<sub>2</sub>/CoS (28.3%) and CoS (22.0%) under the same conditions. This result indicates that CoS<sub>2</sub>/CoS/Ti<sub>3</sub>C<sub>2</sub> has better photocatalytic properties, which may be related to the formation of the built-in potential in CoS<sub>2</sub>/CoS and Schottky junctions between cobalt sulfide and titanium carbide that facilitates the transmission of photo-generated electrons. The removal capacity of different substrates was also examined, which may be directly related to practical applications. As shown in the Figure 6f, sulfadiazine (SDZ) and bisphenol A (BPA) showed similar removal performance as SMT, and the reaction rate constants for SDZ and BPA are 0.023 and 0.021 min<sup>-1</sup>, respectively, indicating that the CoS<sub>2</sub>/CoS/Ti<sub>3</sub>C<sub>2</sub>-cathode is suitable for the removal of antibiotic contaminants and has

good potential for industrial applications. All of these results show that CoS<sub>2</sub>/CoS/Ti<sub>3</sub>C<sub>2</sub> has excellent photo-assisted EF performance.

To further illustrate the mechanism of the PEF process, we drop-casted CoS<sub>2</sub>, CoS<sub>2</sub>/CoS, and CoS<sub>2</sub>/CoS/Ti<sub>3</sub>C<sub>2</sub> nanomaterials on disk ring-electrode without carbon addition and tested the materials selectivity and activity for two-electron oxygen reduction in alkaline solutions (KOH, 0.1 M) without interference from carbon [16]. The electrocatalytic activity was examined by CV in O<sub>2</sub> saturated electrolyte for all three materials (Figure 7a). Compared with CoS<sub>2</sub> (−1.08 V) and CoS/CoS<sub>2</sub> (−1.05 V), the larger oxygen reduction potential (−1.0 V) and double-layer current value of CoS/CoS<sub>2</sub>/Ti<sub>3</sub>C<sub>2</sub> indicate its better activity, which may be due to the presence of Ti<sub>3</sub>C<sub>2</sub> and built-in potential in CoS<sub>2</sub>/CoS accelerate the charge transfer, thereby accelerating the formation of OOH\* (Equation (2)), and OOH\* reacts with H<sup>+</sup> to form H<sub>2</sub>O<sub>2</sub> as the Equation (3). The oxidation peaks at −0.55 V can be ascribed to the oxidation of Co<sup>2+</sup>, and Co<sup>3+</sup> was further converted to Co<sup>2+</sup> when it became electrons at the cathode [13]. As the oxidation of Co(II), the sulfide with metal defects is formed on the catalyst surface, which can be further oxidized to generate sulfur intermediate products (S<sub>2</sub>O<sub>3</sub><sup>2−</sup>, S<sub>2</sub>O<sub>4</sub><sup>2−</sup>), thus, the peaks at 0.166 V could be due to the formation of intermediate sulfides, and these sulfur oxides could be further activated to produce sulfate radicals [40,41]. These results prove that CoS<sub>2</sub>/CoS/Ti<sub>3</sub>C<sub>2</sub> has excellent redox activity, which can be used as the EF cathode to facilitate the produce of active species. The electron transfer capability of the material was studied by Nyquist plots. The impedance test results are shown in Figure 7b, compared with pure CoS and CoS<sub>2</sub>, and CoS<sub>2</sub>/CoS significantly reduces the electron transfer resistance, which is attributed to the built-in potential in CoS<sub>2</sub>/CoS heterojunction helps to increase the charge mobility. After compounding with titanium carbide, the conductivity of CoS/CoS<sub>2</sub>/Ti<sub>3</sub>C<sub>2</sub> material is further improved, which is due to the excellent conductivity of titanium carbide [22].

LSVs of all the catalysts at different speed are depicted in Figure S3a–c. According to the Koutecky-Levich (K-L) formula, the number of electrons transfer (n) for the ORR is calculated (Text S1) [28]. The number of electrons transfer is calculated to be 2.85, 2.12, and 2.22 for CoS<sub>2</sub>, CoS<sub>2</sub>/CoS, and CoS<sub>2</sub>/CoS/Ti<sub>3</sub>C<sub>2</sub>, respectively, demonstrating that CoS<sub>2</sub>/CoS/Ti<sub>3</sub>C<sub>2</sub> has a tendency to 2e<sup>−</sup> ORR process, which is attributed to that built-in potential formed by the heterostructure helps to accelerate the electron migration rate, thus promoting the formation of OOH\* on the CoS<sub>2</sub> surface. Although the number (2.22) of electron transfer after composite Ti<sub>3</sub>C<sub>2</sub> is reduced according to the K-L equation, CoS<sub>2</sub>/CoS/Ti<sub>3</sub>C<sub>2</sub> exhibits a positive onset potential of −0.13 V vs. SCE (Figure S3d), which is higher than that of CoS<sub>2</sub>/CoS (−0.16 V), indicating that Ti<sub>3</sub>C<sub>2</sub> can enhance the electrocatalytic activity of CoS<sub>2</sub>. In addition, rotating ring disk electrode (RRDE) tests of CoS<sub>2</sub>/CoS/Ti<sub>3</sub>C<sub>2</sub>-casted disk from 0.2 V to −1 V vs. SCE at 50 mV/s and different rotational speed were recorded in Figure 7c, and corresponding H<sub>2</sub>O<sub>2</sub> selectivity (p) and the n value are calculated on the basis of Equations (S3) and (S4). The H<sub>2</sub>O<sub>2</sub> selectivity of CoS<sub>2</sub>/CoS/Ti<sub>3</sub>C<sub>2</sub> up to about 76% and remained above 70% over a wide potential range (Figure 7d), and the polarization curves of the CoS<sub>2</sub>/CoS/Ti<sub>3</sub>C<sub>2</sub> show about 0.75 V vs. RHE of half-wave potential, which is close to thermodynamic limit of two-electron ORR. Apart from the high activity, the stability tests of the material are shown in Figure 7e, with a ring voltage setting of 1.48 V and disc voltage of 0.5 V, the i-t test of CoS<sub>2</sub>/CoS/Ti<sub>3</sub>C<sub>2</sub> material showed excellent stability with a stable H<sub>2</sub>O<sub>2</sub> selectivity of about 70% within 2 h. The above results indicate that CoS<sub>2</sub>/CoS/Ti<sub>3</sub>C<sub>2</sub> has excellent 2e<sup>−</sup> ORR activity and stability, and 2e<sup>−</sup> ORR is uptaken at low overpotentials.

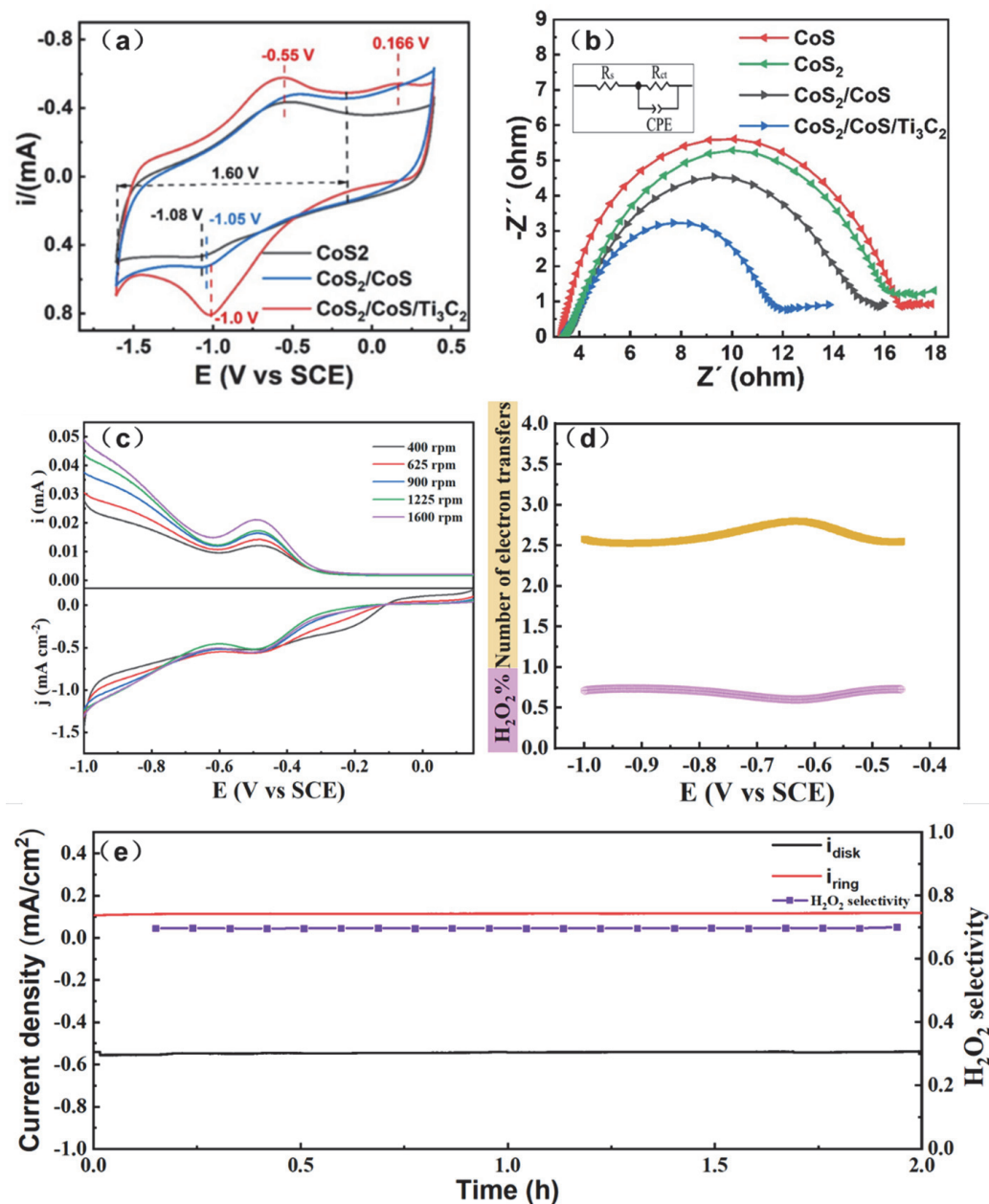
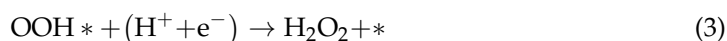


**Figure 7.** (a) CV of CoS<sub>2</sub>, CoS<sub>2</sub>/CoS, and CoS<sub>2</sub>/CoS/Ti<sub>3</sub>C<sub>2</sub> in O<sub>2</sub>-saturated electrolyte. (b) EIS plots of different samples. (c) LSVs of CoS<sub>2</sub>/CoS/Ti<sub>3</sub>C<sub>2</sub> performed with RRDE test in O<sub>2</sub>-saturated. (d) The H<sub>2</sub>O<sub>2</sub> selectivity and number of electron transfers, (e) i-t curve of disc-ring electrode at 1600 rpm.

The photo adsorption properties of different samples were analyzed by UV-Vis DRS (Figure 8a). CoS exhibits strong light absorption in the ultraviolet and visible regions (edge of approximately 450 nm and 280 nm), and CoS<sub>2</sub>/CoS and CoS<sub>2</sub>/CoS/Ti<sub>3</sub>C<sub>2</sub> display stronger absorption in the scope of 280–700 nm. The tauc plot method (Figure 8b) is used to fit the light absorption value as the Equation (1). The band gap of CoS<sub>2</sub>/CoS/Ti<sub>3</sub>C<sub>2</sub> (~1.95 eV) is slightly lower than that of CoS (~2.25 eV) and CoS<sub>2</sub>/CoS (~2.06 eV), which indicates that the heterostructure of CoS<sub>2</sub>/CoS and the schottky junction formed under the modification of Ti<sub>3</sub>C<sub>2</sub> broaden the light absorption range of the material, which helps to absorb more visible light to further improve the catalytic activity. Furthermore, the photocurrent curve (Figure 8c) is used to analyze the electron-hole separation efficiency of the materials. Compared with CoS and CoS<sub>2</sub>/CoS, CoS<sub>2</sub>/CoS/Ti<sub>3</sub>C<sub>2</sub> show higher photocurrent intensity and stronger photo response performance, which is attributed to the electron withdrawing effect of Ti<sub>3</sub>C<sub>2</sub> facilitating the separation of photo-generated holes and

electrons [42], moreover, the built-in potential in the heterojunction also helps to accelerate the transfer of electrons. PL spectrum (Figure 8d) also proves this fact, and the lowest PL peak of CoS<sub>2</sub>/CoS/Ti<sub>3</sub>C<sub>2</sub> indicates that photo-generated electron recombination is well suppressed, which helps to extend the life of photo-generated carriers and holes, thereby improving photocatalytic activity. There is a significant gap in the removal capacity of SMT under light (98.5%) and dark (89%) conditions, respectively (Figure 6e). Under the condition of only light, the effective removal of SMT is about 34.5% within 120 min. The above facts illustrate that CoS<sub>2</sub>/CoS/Ti<sub>3</sub>C<sub>2</sub> have excellent photo-assisted electrocatalytic activity.

$$(\alpha h\nu)^{1/n} = A(h\nu - E_g) \quad (1)$$



Electron paramagnetic resonance (EPR) was conducted by the spin trap agents of 5,5-dimethyl-1-pyrroline N-oxide (DMPO) to confirm the existence of various reactive oxide species in this reaction process. The result is shown in Figure 9a, and weak DMPO-·OH signal can be observed under only light conditions, which is attributed to the interaction of photogenerated electrons with ·O<sub>2</sub><sup>-</sup> to produce ·OH as the Equations (4)–(7). Therefore, the removal of SMT under light conditions alone may be attributed to the ·O<sub>2</sub><sup>-</sup> (−0.33 eV). After turning on the power, obvious signals of four peaks with the intensity value of 1:2:2:1 (DMPO-·OH) adducts can be found in the EPR spectrum [43], indicating that the existence of ·OH in CoS<sub>2</sub>/CoS/Ti<sub>3</sub>C<sub>2</sub> system under PEF condition. Furthermore, the weak characteristic peaks of DMPO-SO<sub>4</sub><sup>-</sup> also could be detected, which is due to the oxidation of S<sup>2-</sup> and SO<sub>4</sub><sup>2-</sup> in the solution to sulfur oxides (such as S<sub>2</sub>O<sub>3</sub><sup>2-</sup>, S<sub>2</sub>O<sub>4</sub><sup>2-</sup>), and then sulfur oxides could be further activated to produce SO<sub>4</sub><sup>-</sup>, and the high oxidation potential (2.7~3.1 eV) of SO<sub>4</sub><sup>-</sup> can also effectively promote the degradation of the substrates (Figure 9b). Six characteristic peaks of DOMP-·O<sub>2</sub><sup>-</sup> compounding are observed, suggesting the production of ·O<sub>2</sub><sup>-</sup> under the action of light and electricity (Figure 9c). Quenching experiments were performed to clarify the contribution of different ROS in this PEF system. TBA and MeOH act as the trapping agents of ·OH and SO<sub>4</sub><sup>-</sup>, respectively. Figure 9d showed that SMT decay rate is significantly inhibited when TBA (100 mM) is added, and the degradation performance is as low as 50.5% in 120 min, indicating the major roles of ·OH in reaction system. In the presence of MeOH (100 mM), the decay rate of SMT still remains around 71.2%, indicating that SO<sub>4</sub><sup>-</sup> has a relatively low contribution for degradation process, therefore, the ·OHs are critical to the degradation performance in the CoS<sub>2</sub>/CoS/Ti<sub>3</sub>C<sub>2</sub> system. Anti-ion interference experiments were also carried out, as shown in Figure S6. It can be seen that NO<sub>3</sub><sup>-</sup> and Cl<sup>-</sup> have little effect on the degradation process of SMT, however, the presence of HCO<sub>3</sub><sup>-</sup> makes the removal efficiency of SMT slightly lower (about 20%), but it is undeniable that even in the presence of anions, the removal rate of SMT is still more than 70%, which indicates that the CoS<sub>2</sub>/CoS/Ti<sub>3</sub>C<sub>2</sub> cathode system has a better ability for resistance to ion interference. Based on the above results, the CoS<sub>2</sub>/CoS/Ti<sub>3</sub>C<sub>2</sub> cathode system can effectively produce active radicals under EF conditions, and the degradation performance was further enhanced by the addition of light. Compared with FeS<sub>2</sub>NWs/Ti<sub>3</sub>C<sub>2</sub> cathode 28, CoS<sub>2</sub>/CoS/Ti<sub>3</sub>C<sub>2</sub> showed higher 2e<sup>-</sup> ORR catalytic activity, higher TOC removal rate (76%), and greater PEF catalytic performance owing to the uneven charge distribution of CoS<sub>2</sub>/CoS heterojunction. Moreover, due to the excellent 2e<sup>-</sup> ORR properties of the CoS<sub>2</sub>/CoS/Ti<sub>3</sub>C<sub>2</sub> material, the addition of reduced graphene oxide (RGO) is effectively avoided.

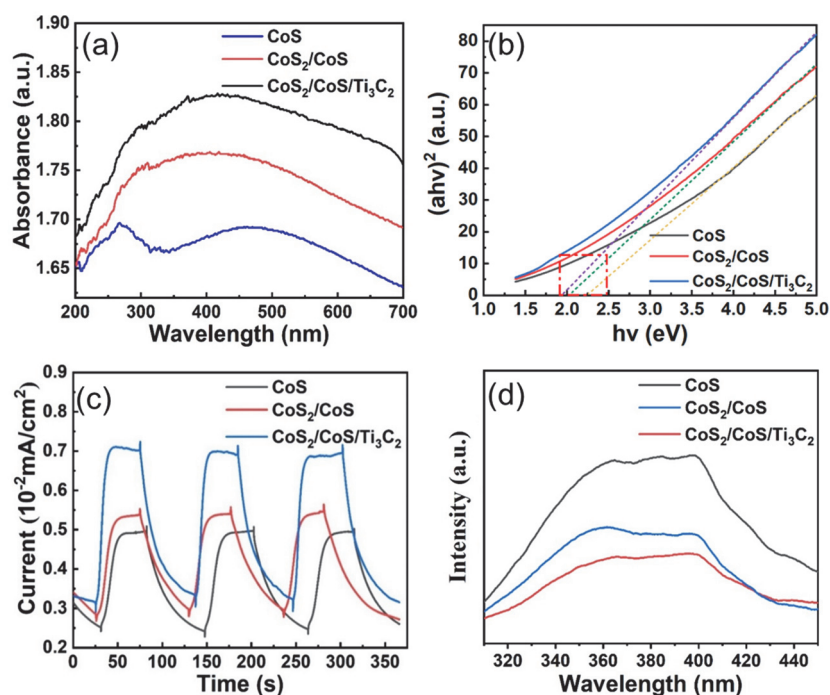


**Figure 8.** (a) DRS spectra, (b) the corresponding Tauc plots (the colored dotted lines are tangents to the corresponding solid lines), (c) transient photocurrent responses, and (d) PL spectrum of CoS, CoS<sub>2</sub>/CoS, CoS<sub>2</sub>/CoS/Ti<sub>3</sub>C<sub>2</sub>.

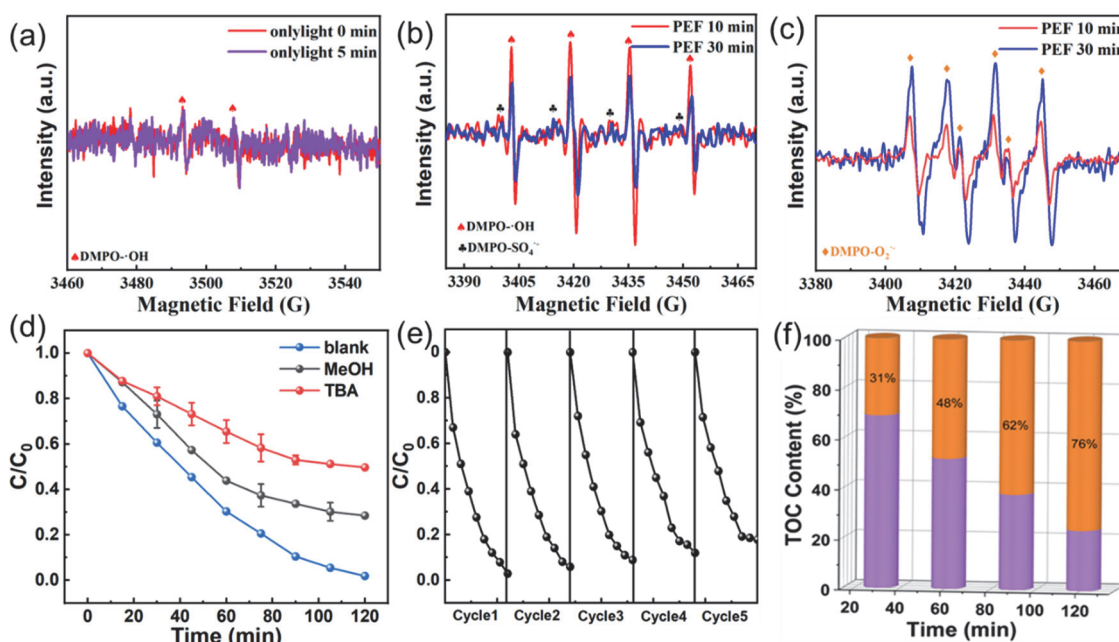
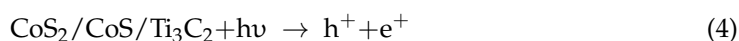


**Figure 9.** (a) DMPO-OH spin-trapping EPR spectra in the condition of (a) only light, (b) PEF, (c) DMPO-O<sub>2</sub><sup>-</sup> spin-trapping EPR spectra, (d) quenching experiment, (e) cycle performance, (f) TOC removal rate.

The stability and long-term runnability of the cathode are essential factors in assessing the ability of the material to perform in real-world applications. The removal efficiency of SMT by the CoS<sub>2</sub>/CoS/Ti<sub>3</sub>C<sub>2</sub> cathode after five cycle tests is well preserved (Figure 9e), decreasing by about 14.5% compared with that for the first cycle. The main reasons for the performance decay of the CoS<sub>2</sub>/CoS/Ti<sub>3</sub>C<sub>2</sub> cathode may be that deactivation of functional group of Ti<sub>3</sub>C<sub>2</sub> due to the occupation of the active site by contaminants, and quality loss of

CoS<sub>2</sub>/CoS/Ti<sub>3</sub>C<sub>2</sub> due to sulfide being further oxidized to sulfur oxides (such as S<sub>2</sub>O<sub>3</sub><sup>2-</sup>, S<sub>2</sub>O<sub>4</sub><sup>2-</sup>) [40,41]. Despite this, the performance remained around 85% after five cycles, indicating its excellent stability. Figure 9f shows the variation of total organic carbon content with time in SMT degradation process. As the reaction time increased from 30 to 120 min, the mineralization rate of SMT by the CoS<sub>2</sub>/CoS/Ti<sub>3</sub>C<sub>2</sub> cathode PEF system increased from 31% to 76%. The high mineralization rate is ascribed to the oxidation of reactive oxygen species ( $\cdot\text{O}_2^-$ ,  $\cdot\text{OH}$ ,  $\text{SO}_4^-$ ). Stability of the catalysts in water treatment system is crucial for their engineering applications. To further reveal the element features of the used catalyst, XRD and XPS of used CoS<sub>2</sub>/CoS/Ti<sub>3</sub>C<sub>2</sub> were presented in Figure S5. The XRD feature of the used catalyst still has the characteristic peaks of cobalt sulfide, but the corresponding peak intensity is reduced, which may be related to the adsorption of binder polymers and contaminants on the catalyst sites. Moreover, the reusability of the electrode was confirmed through the XPS results of the electrode before and after cycle. The XPS spectrum of Figure S5b shows that the used catalyst has similar characteristics to the fresh CoS<sub>2</sub>/CoS/Ti<sub>3</sub>C<sub>2</sub> catalyst, and the characteristic peaks corresponding to Co 2p and S 2p are weakened (Figure S6c,d), which may be due to the inevitable ion leaching and sulfide being further oxidized to intermediate sulfur oxides in acidic conditions, and then sulfur oxides could be further activated to produce  $\text{SO}_4^-$  to promote the degradation of the SMT. Thus, CoS<sub>2</sub>/CoS/Ti<sub>3</sub>C<sub>2</sub> can be considered as an effective PEF cathode material for more thorough removal of pollutants.



To clarify the degradation pathway of SMT in the CoS<sub>2</sub>/CoS/Ti<sub>3</sub>C<sub>2</sub> system, the transformation products of SMT were analyzed by QTOF LC/MS (UPLC-M-QTOF). The proposed intermediate compounds are shown in Figure S7. SMT was attacked by  $\cdot\text{O}_2^-$ ,  $\text{SO}_4^-$  and  $\cdot\text{OH}$  to form intermediate products, and the reaction pathway (Figure 10) included (1) oxidation process of aniline group in SMT to produce N-(4-methylpyrimidin-2-yl)-4-(hydroxyamino)-benzenesulfonamide (P1, m/z, 281.0) and N-(4-methylpyrimidin-2-yl)-4-nitrobenzene-sulfonamide (P1-1, m/z, 296.1). (2) The attack of ROS could lead to the cleavage of S–N bond to form 4-methylpyrimidin-2-amine (P2, m/z, 110.2) and 4-aminobenzenesulfonic acid, which was further oxidized to form 4-nitrobenzenesulfonic acid (P2-1, m/z, 203.1) [44], and this result was frequently reported in AOPs-based water treatment processes for the degradation of sulfonamide antibiotics [45]. (3) Smiles-type rearrangement of SMT to generate 4-(2-imino-4-methylpyrimidin-1(2H)-yl) aniline, which was further oxidized to form 4-methyl-1-(4-nitrosophenyl) pyrimidin-2(1H)-imine (P3, m/z, 214.9) and 4-methyl-1-(4-nitrophenyl) pyrimidin-2(1H)-imine, (P3-1, m/z, 232.9). (4) The SO<sub>2</sub> extrusion of SMT or the oxidation of P3-1 resulted in the formation of nitrobenzene (P4, m/z, 124.9), which could be further oxidized to phenol (P4-1, m/z, 94.9). The intermediate products generated above will become smaller molecules through dealkylation and ring-opening reactions under the action of ROS, and ultimately, the above intermediates could be partially mineralized to carbon dioxide and water.

Given the above results, mechanism of CoS<sub>2</sub>/CoS/Ti<sub>3</sub>C<sub>2</sub> cathode for removal of micro-pollutants was proposed. The energy of E<sub>VB</sub> and E<sub>CB</sub> of CoS<sub>2</sub>/CoS/Ti<sub>3</sub>C<sub>2</sub> are calculated according to Equations (8) and (9) [46]. According to the calculation results, the values of E<sub>VB</sub> and E<sub>CB</sub> are 1.79 eV and −0.46 eV, respectively. Under visible light irradiation, electrons are generated in CB and holes are generated in VB of CoS. Due to the electron-absorbing properties of Ti<sub>3</sub>C<sub>2</sub>, the conducting electrons of CoS are further transferred to the surface of it, which facilitates the separation of holes and electrons. The electrons in the Ti<sub>3</sub>C<sub>2</sub> could reduce O<sub>2</sub> to generate  $\cdot\text{O}_2^-$  (−0.33 eV) [42]. At the same time, the continuously

generated  $e^-$  and  $h^+$  could make the CB and VB bend upward, establishing Schottky barriers through the contact interface and facilitating the separation of photo-generated electrons and holes [28,46]. In addition,  $O_2$  is rapidly converted to produce  $H_2O_2$  on the  $CoS_2/CoS/Ti_3C_2$  surface as Equations (5) and (6). The generated  $H_2O_2$  is then activated on the surface of  $CoS_2/CoS/Ti_3C_2$  and participated in the activated process to generate  $\cdot OH$  as the Equation (10). Due to the synergistic effect of  $S^{2-}$  and Co, Co(II) can be regenerated on the surface of the cathode (Equation (11)) [18,19]. In addition, decomposition of  $H_2O_2$  (Equation (7)) can be improved under irradiation. Sulfate in the solution can be oxidized to form persulfate, which is further activated to produce sulfate radicals [13, 41,42]. Therefore, the ROS produced in the PEF process could attack functional groups of contaminants quickly and effectively.

$$E_{VB} = \chi - E_e + 0.5E_g \quad (8)$$

$$E_{CB} = E_{VB} - E_g \quad (9)$$

where  $\chi$  is the absolute electronegativity of the semiconductor.  $E_e$  is the energy of free electrons on the hydrogen scale (4.50 eV).  $E_g$  is the band gap of the semiconductor [20].

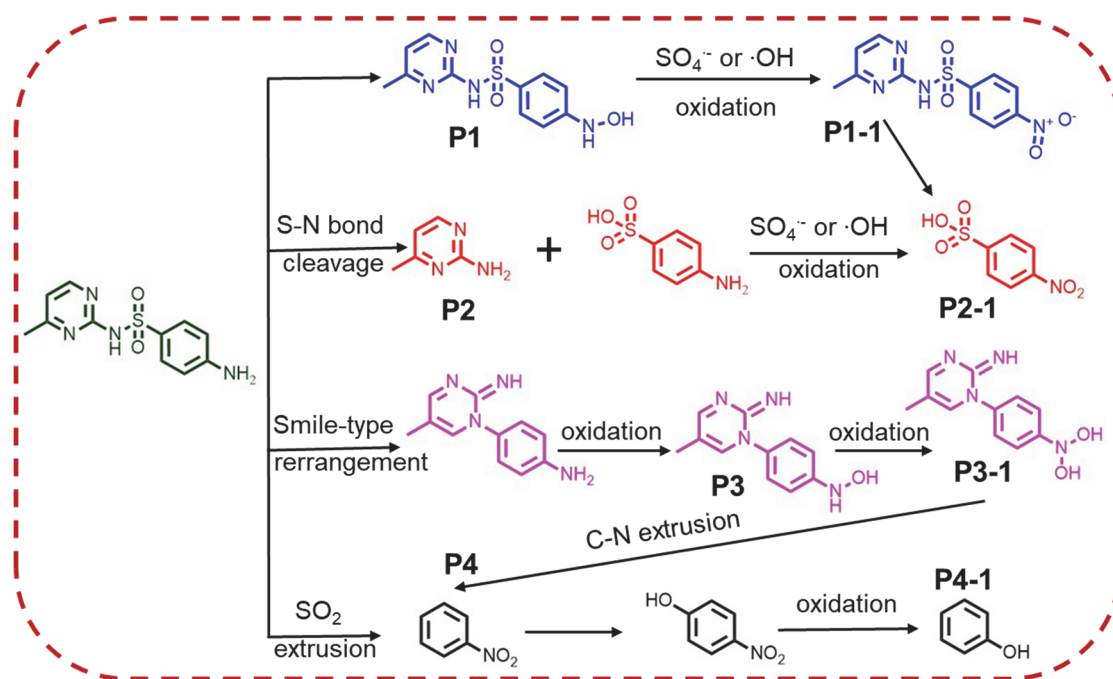
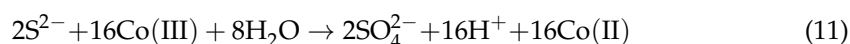


**Figure 10.** Proposed reaction pathway for the oxidation of SMT at ambient pH by  $CoS_2/CoS/Ti_3C_2$  cathode system.

### 3. Experimental Section

#### 3.1. Chemicals

Cobalt sulfate heptahydrate ( $CoSO_4 \cdot 7H_2O$ , 99.99%), urea ( $CH_4N_2O$ , 99.5%), sublimed sulfur (S, 99.5%), ethylene glycol ( $(CH_2OH)_2$ , 98%), N, N-Dimethylformamide ( $C_3H_7NO$ , 99.8%), tetramethylammonium hydroxide solution ( $C_4H_{13}NO$ , 25%), titanium aluminum carbide powder ( $Ti_3AlC_2$ , 98%), tert-butanol (TBA, 99.5%), and methanol (MeOH, 99.5%) are chemicals, which were all purchased from Aladdin Chemical Reagent Co., Ltd. (Shanghai, China), unless otherwise stated.

### 3.2. Preparation of CoS<sub>2</sub>/CoS and CoS<sub>2</sub>/CoS/Ti<sub>3</sub>C<sub>2</sub>

In the typical procedure, 10 mmol urea, 2 mmol CoSO<sub>4</sub>, and 25 mmol sulfur powder were added to 60 mL mixture solution of DMF and EG. The mixture solution was stirred for 30 min and then sonicated for 30 min. The well mixed precursor solution is added to Teflon-lined autoclave. The solution is maintained in an automatic heating oven at 180 °C for 12 h. After the hydrothermal reaction, the sample was naturally cooled to room temperature, centrifuged, and washed three times with ethanol and ultrapure water. The samples were dried under vacuum. The CoS<sub>2</sub>, CoS<sub>2</sub>/CoS, and CoS were obtained under the conditions of V<sub>EG</sub>:V<sub>DMF</sub> = 0.5, 0.9, and 2.0.

Ti<sub>3</sub>AlC<sub>2</sub> was etched in HF solution to obtain Ti<sub>3</sub>C<sub>2</sub>. Subsequently, the 25% TMAOH solution was used to intercalate Ti<sub>3</sub>C<sub>2</sub> to obtain a monolithic layer of Ti<sub>3</sub>C<sub>2</sub>. Similarly, to obtain CoS<sub>2</sub>/CoS/Ti<sub>3</sub>C<sub>2</sub>, (50 mg) of stripped Ti<sub>3</sub>C<sub>2</sub> was placed in a mixed solution, and the temperature was maintained at 180 °C for 12 h. After centrifugal washing, the sample is vacuum dried.

### 3.3. Characterization and Experimental Process

Detailed information of preparation of CoS<sub>2</sub>/CoS/Ti<sub>3</sub>C<sub>2</sub> cathode and degradation test was shown in Supplementary Materials Text S2.

## 4. Conclusions

In summary, CoS<sub>2</sub>/CoS/Ti<sub>3</sub>C<sub>2</sub> displayed a superior catalytic performance in photo-assisted-electro-Fenton process compared with other materials (Table S3). The charged surface derived from the built-in potential benefited to facilitate the electron migration. Both the oxygen reduction ability for 2e<sup>-</sup> process and photogenerated electron-hole separation of CoS<sub>2</sub>/CoS/Ti<sub>3</sub>C<sub>2</sub> were enhanced owing to the uneven charge distribution of CoS<sub>2</sub>/CoS heterojunction. CoS<sub>2</sub>/CoS/Ti<sub>3</sub>C<sub>2</sub> cathode demonstrated a high PEF performance with 98.5% degradation rate for SMT at 20 mA/cm<sup>2</sup> within 120 min and excellent performance retention of 85% after five cycles. Moreover, ESR signals revealed that the main ROS in the degradation process of SMT was ·OH. The design and construction of photoelectric Fenton electrocatalysts with heterojunction offers a promising strategy to enhance the performance and competitiveness. In addition, based on the excellent catalytic performance of this material, further research with various substrates (such as other Mxenes materials) is undergoing to further improve the water splitting process and broaden the application scope of CoS<sub>2</sub>/CoS-based materials.

**Supplementary Materials:** The following supporting information can be downloaded at: <https://www.mdpi.com/article/10.3390/catal13020253/s1>, Figure S1. Morphology of Ti<sub>3</sub>C<sub>2</sub> sample after etching with hydrofluoric acid. Figure S2. TEM of (a) CoS<sub>2</sub>/CoS (b) CoS<sub>2</sub>/CoS/Ti<sub>3</sub>C<sub>2</sub>. Figure S3. LSVs of (a) CoS<sub>2</sub>, (b) CoS<sub>2</sub>/CoS, (c) CoS<sub>2</sub>/CoS/Ti<sub>3</sub>C<sub>2</sub> performed with RDE test in O<sub>2</sub>-saturated (697 μg/cm<sup>2</sup>) and the corresponding K-L curves (inset), (d) LSVs of CoS<sub>2</sub>/CoS and CoS<sub>2</sub>/CoS/Ti<sub>3</sub>C<sub>2</sub>. Figure S4. pseudo first order reaction rate of different substrates in CoS<sub>2</sub>/CoS/Ti<sub>3</sub>C<sub>2</sub> cathode system. Figure S5. (a) XRD pattern and (b-d) XPS of used CoS<sub>2</sub>/CoS/Ti<sub>3</sub>C<sub>2</sub> catalyst. Figure S6. Resistance to ion interference of CoS<sub>2</sub>/CoS/Ti<sub>3</sub>C<sub>2</sub> cathode Figure S7. MS spectrum of intermediate products in SMT degradation process. Table S1. Performance comparison with similar materials. References [47–51] are cited in Supplementary Materials.

**Author Contributions:** Data curation, F.C. and H.L.; Formal analysis, F.C. and F.Y.; Funding acquisition, Y.L.; Methodology, F.C. and Z.W.; Resources, S.C.; Software, N.C. and Z.W.; Validation, F.Y. and Y.L.; Writing—review and editing, F.C., F.Y. and S.C. All authors have read and agreed to the published version of the manuscript.

**Funding:** This work was funded by the National Natural Science Foundation of China, grant number No. 21776308.

**Data Availability Statement:** All the relevant data used in this study have been provided in the form of figures and tables in the published article, and all data provided in the present manuscript are available to whom it may concern.

**Conflicts of Interest:** The authors declare no conflict of interest.

## References

1. Cheng, S.; Shen, C.; Zheng, H.; Liu, F.; Li, A. OCNs encapsulating Fe-Co PBA as efficient chainmail-like electrocatalyst for enhanced heterogeneous electro-Fenton reaction. *Appl. Catal. B* **2020**, *269*, 118–785. [[CrossRef](#)]
2. Zhu, Y.; Zhu, R.; Xi, Y.; Zhu, J.; Zhu, G.; He, H. Strategies for enhancing the heterogeneous Fenton catalytic reactivity: A review. *Appl. Catal. B* **2019**, *255*, 117–739. [[CrossRef](#)]
3. Ganiyu, S.O.; Huong, L.T.X.; Bechelany, M.; Esposito, G.; van Hullebusch, E.D.; Oturan, M.A.; Cretin, M. A hierarchical CoFe-layered double hydroxide modified carbon-felt cathode for heterogeneous electro-Fenton process. *J. Mater. Chem. A* **2017**, *5*, 3655–3666. [[CrossRef](#)]
4. Haider, M.R.; Jiang, W.L.; Han, J.L.; Sharif, H.M.A.; Ding, Y.C.; Cheng, H.Y.; Wang, A.J. In-situ electrode fabrication from polyaniline derived N-doped carbon nanofibers for metal-free electro-Fenton degradation of organic contaminants. *Appl. Catal. B* **2019**, *256*, 117–774. [[CrossRef](#)]
5. Zhang, C.; Li, F.; Wen, R.; Zhang, H.; Elumalai, P.; Zheng, Q.; Chen, H.; Yang, Y.; Huang, M.; Ying, G. Heterogeneous electro-Fenton using three-dimension NZVI-BC electrodes for degradation of neonicotinoid wastewater. *Water Res.* **2020**, *182*, 115975. [[CrossRef](#)]
6. Chu, L.; Sun, Z.; Fang, G.; Cang, L.; Wang, X.; Zhou, D.; Gao, J. Highly effective removal of BPA with boron-doped graphene shell wrapped FeS<sub>2</sub> nanoparticles in electro-Fenton process: Performance and mechanism. *Sep. Purif. Technol.* **2021**, *267*, 118–680. [[CrossRef](#)]
7. Qin, X.; Zhao, K.; Quan, X.; Cao, P.; Chen, S.H. Highly efficient metal-free electro-Fenton degradation of organic contaminants on a bifunctional catalyst. *J. Hazard. Mater.* **2021**, *416*, 125859. [[CrossRef](#)]
8. Cheng, S.; Zheng, H.; Shen, C.; Jiang, B.; Liu, F.; Li, A. Hierarchical Iron Phosphides Composite Confined in Ultrathin Carbon Layer as Effective Heterogeneous Electro-Fenton Catalyst with Prominent Stability and Catalytic Activity. *Adv. Funct. Mater.* **2021**, *31*, 2106311. [[CrossRef](#)]
9. Wang, H.; Wang, Y.; Zhang, J.; Liu, X.; Tao, S. Electronic structure engineering through Fe-doping CoP enables hydrogen evolution coupled with electro-Fenton. *Nano Energy* **2021**, *84*, 105–943. [[CrossRef](#)]
10. Yu, D.; He, J.; Wang, Z.; Pang, H.; Li, L.; Chen, Y.; Zheng, Y.; Zhang, J. Mineralization of norfloxacin in a CoFe-LDH/CF cathode-based heterogeneous electro-fenton system: Preparation parameter optimization of the cathode and conversion mechanisms of H<sub>2</sub>O<sub>2</sub> to ·OH. *Chem. Eng. J.* **2021**, *417*, 129–240. [[CrossRef](#)]
11. Zhang, D.; Yin, K.; Tang, Y.; Wei, Y.; Tang, H.; Du, Y.; Liu, H.; Chen, Y.; Liu, C. Hollow sea-urchin-shaped carbon-anchored single-atom iron as dual-functional electro-Fenton catalysts for degrading refractory thiamphenicol with fast reaction kinetics in a wide pH range. *Chem. Eng. J.* **2022**, *427*, 130–996. [[CrossRef](#)]
12. Dong, P.; Chen, X.; Guo, M.; Wu, Z.; Wang, H.; Lin, F.; Zhang, J.; Wang, S.; Sun, C.; Zhao, H. Heterogeneous electro-Fenton catalysis with self-supporting CFP@MnO<sub>2</sub>-Fe<sub>3</sub>O<sub>4</sub>/C cathode for shale gas fracturing flowback wastewater. *J. Hazard. Mater.* **2021**, *412*, 125–208. [[CrossRef](#)]
13. Guo, M.; Lu, M.; Zhao, H.; Lin, F.; He, F.; Zhang, J.; Wang, S.; Dong, P.; Zhao, C. Efficient electro-Fenton catalysis by self-supported CFP@CoFe<sub>2</sub>O<sub>4</sub> electrode. *J. Hazard. Mater.* **2022**, *423*, 127033. [[CrossRef](#)] [[PubMed](#)]
14. Zhang, M.; Gong, Y.; Ma, N.; Zhao, X. Promoted photoelectrocatalytic degradation of BPA with peroxymonosulfate on a MnFe<sub>2</sub>O<sub>4</sub> modified carbon paper cathode. *Chem. Eng. J.* **2020**, *399*, 125088. [[CrossRef](#)]
15. Guo, M.; Qayum, A.; Dong, S.; Jiao, X.; Chen, D.; Wang, T. In situ conversion of metal (Ni, Co or Fe) foams into metal sulfide (Ni<sub>3</sub>S<sub>2</sub>, Co<sub>9</sub>S<sub>8</sub> or FeS) foams with surface grown N-doped carbon nanotube arrays as efficient superaerophobic electrocatalysts for overall water splitting. *J. Mater. Chem. A* **2020**, *8*, 9239–9247. [[CrossRef](#)]
16. Sheng, H.; Hermes, E.D.; Yang, X.; Ying, D.; Janes, A.N.; Li, W.; Schmidt, J.R. Electrocatalytic Production of H<sub>2</sub>O<sub>2</sub> by Selective Oxygen Reduction Using Earth-Abundant Cobalt Pyrite (CoS<sub>2</sub>). *ACS Catal.* **2019**, *9*, 8433–8442. [[CrossRef](#)]
17. Kim, M.; Kim, S.H.; Lee, J.H.; Kim, J. Unravelling lewis acidic and reductive characters of normal and inverse nickel-cobalt thiospinels in directing catalytic H<sub>2</sub>O<sub>2</sub> cleavage. *J. Hazard. Mater.* **2020**, *392*, 122347. [[CrossRef](#)]
18. Ding, Y.; Hu, Y.; Peng, X.; Xiao, Y.; Huang, J. Micro-nano structured CoS: An efficient catalyst for peroxymonosulfate activation for removal of bisphenol A. *Sep. Purif. Technol.* **2020**, *233*, 116022. [[CrossRef](#)]
19. Yein, W.T.; Wang, Q.; Wu, J.; Wu, X. Converting CoS-TEA hybrid compound to CoS defective ultrathin nanosheets and their enhanced photocatalytic property. *J. Mol. Liq.* **2018**, *268*, 273–283. [[CrossRef](#)]
20. Zhao, W.; Feng, Y.; Huang, H.; Zhou, P.; Li, J.; Zhang, L.; Dai, B.; Xu, J.; Zhu, F.; Sheng, N.; et al. A novel Z-scheme Ag<sub>3</sub>VO<sub>4</sub>/BiVO<sub>4</sub> heterojunction photocatalyst: Study on the excellent photocatalytic performance and photocatalytic mechanism. *Appl. Catal. B* **2019**, *245*, 448–458. [[CrossRef](#)]
21. Li, Y.; Zhao, Q.; Zhang, Y.; Li, Y.; Fan, L.; Li, F.T.; Li, X. In-situ construction of sequential heterostructured CoS/CdS/CuS for building “electron-welcome zone” to enhance solar-to-hydrogen conversion. *Appl. Catal. B* **2022**, *300*, 120–763. [[CrossRef](#)]
22. Ma, D.; Hu, B.; Wu, W.; Liu, X.; Zai, J.; Shu, C.; Tadesse Tsega, T.; Chen, L.; Qian, X.; Liu, T.L. Highly active nanostructured CoS<sub>2</sub>/CoS heterojunction electrocatalysts for aqueous polysulfide/iodide redox flow batteries. *Nat. Commun.* **2019**, *10*, 3367. [[CrossRef](#)] [[PubMed](#)]
23. Shi, Y.; Wang, X.; Liu, X.; Ling, C.; Shen, W.; Zhang, L. Visible light promoted Fe<sub>3</sub>S<sub>4</sub> Fenton oxidation of atrazine. *Appl. Catal. B* **2020**, *277*, 119–229. [[CrossRef](#)]

24. Zhao, R.; Qian, Z.; Liu, Z.; Zhao, D.; Hui, X.; Jiang, G.; Wang, C.; Yin, L. Molecular-level heterostructures assembled from layered black phosphorene and  $\text{Ti}_3\text{C}_2$  MXene as superior anodes for high-performance sodium ion batteries. *Nano Energy* **2019**, *65*, 104037. [[CrossRef](#)]
25. Cheng, L.; Chen, Q.; Li, J.; Liu, H. Boosting the photocatalytic activity of  $\text{CdLa}_2\text{S}_4$  for hydrogen production using  $\text{Ti}_3\text{C}_2$  MXene as a co-catalyst. *Appl. Catal. B* **2020**, *267*, 118–379. [[CrossRef](#)]
26. Liao, Y.; Qian, J.; Xie, G.; Han, Q.; Dang, W.; Wang, Y.; Lv, L.; Zhao, S.; Luo, L.; Zhang, W.; et al. 2D-layered  $\text{Ti}_3\text{C}_2$  MXenes for promoted synthesis of  $\text{NH}_3$  on P25 photocatalysts. *Appl. Catal. B* **2020**, *273*, 119054. [[CrossRef](#)]
27. Ai, Z.; Shao, Y.; Chang, B.; Huang, B.; Wu, Y.; Hao, X. Effective orientation control of photogenerated carrier separation via rational design of a  $\text{Ti}_3\text{C}_2(\text{TiO}_2)@\text{CdS}/\text{MoS}_2$  photocatalytic system. *Appl. Catal. B* **2019**, *242*, 202–208. [[CrossRef](#)]
28. Xia, Y.; Yang, F.; Zhang, B.; Xu, C.; Yang, W.; Li, Y.F. Fabrication of novel  $\text{FeS}_2$  NWs/ $\text{Ti}_3\text{C}_2$  cathode for Photo-Electro-Fenton degradation of sulfamethazine. *Chem. Eng. J.* **2021**, *426*, 130–719.
29. Xu, H.; Cao, J.; Shan, C.; Wang, B.; Xi, P.; Liu, W.; Tang, Y. MOF-Derived Hollow CoS Decorated with  $\text{CeO}_x$  Nanoparticles for Boosting Oxygen Evolution Reaction Electrocatalysis. *Angew. Chem. Int. Ed. Engl.* **2018**, *57*, 8654–8658. [[CrossRef](#)]
30. Al-Musawi, T.J.; Arghavan, S.M.A.; Allahyari, E.; Arghavan, F.S.; Othmani, A.; Nasseh, N. Adsorption of malachite green dye onto almond peel waste: A study focusing on application of the ANN approach for optimization of the effect of environmental parameters. *Biomass Convers. Biorefinery* **2020**, *273*, 119054. [[CrossRef](#)]
31. Nasseh, N.; Samadi, M.T.; Ghadirian, M.; Panahi, A.H.; Rezaie, A. Photo-catalytic degradation of tamoxifen by using a novel synthesized magnetic nanocomposite of  $\text{FeCl}_2@\text{ac}@\text{ZnO}$ : A study on the pathway, modeling, and sensitivity analysis using artificial neural network (AAN). *J. Environ. Chem. Eng.* **2022**, *10*, 107450. [[CrossRef](#)]
32. Rahimi, S.M.; Panahi, A.H.; Allahyari, E.; Nasseh, N. Breaking down of low-biodegradation Acid Red 206 dye using bentonite/ $\text{Fe}_3\text{O}_4/\text{ZnO}$  magnetic nanocomposite as a novel photo-catalyst in presence of UV light. *Chem. Phys. Lett.* **2022**, *794*, 139480. [[CrossRef](#)]
33. Fenton, J.L.; Schaak, R.E. Structure-Selective Cation Exchange in the Synthesis of Zincblende MnS and CoS Nanocrystals. *Angew. Chem. Int. Ed. Engl.* **2017**, *56*, 6464–6467. [[CrossRef](#)] [[PubMed](#)]
34. Sheng, H.; Janes, A.N.; Ross, R.D.; Kaiman, D.; Huang, J.; Song, B.; Schmidt, J.R.; Jin, S. Stable and selective electrosynthesis of hydrogen peroxide and the electro-Fenton process on  $\text{CoSe}_2$  polymorph catalysts. *Energy Environ. Sci.* **2020**, *13*, 4189–4203. [[CrossRef](#)]
35. Kinner, T.; Bhandari, K.P.; Bastola, E.; Monahan, B.M.; Haugen, N.O.; Roland, P.J.; Bigioni, T.P.; Ellingson, R.J. Majority Carrier Type Control of Cobalt Iron Sulfide ( $\text{Co}_x\text{Fe}_{1-x}\text{S}_2$ ) Pyrite Nanocrystals. *J. Phys. Chem. C* **2016**, *120*, 5706–5713. [[CrossRef](#)]
36. Peng, S.; Han, X.; Li, L.; Zhu, Z.; Cheng, F.; Srinivansan, M.; Adams, S.; Ramakrishna, S. Unique Cobalt Sulfide/Reduced Graphene Oxide Composite as an Anode for Sodium-Ion Batteries with Superior Rate Capability and Long Cycling Stability. *Small* **2016**, *12*, 1359–1368. [[CrossRef](#)]
37. Yun, X.; Lu, T.; Zhou, R.; Lu, Z.; Li, J.; Zhu, Y. Heterostructured  $\text{NiSe}_2/\text{CoSe}_2$  hollow microspheres as battery-type cathode for hybrid supercapacitors: Electrochemical kinetics and energy storage mechanism. *Chem. Eng. J.* **2021**, *426*, 131–328. [[CrossRef](#)]
38. Hao, J.; Yang, W.; Peng, Z.; Zhang, C.; Huang, Z.; Shi, W. A nitrogen doping method for  $\text{CoS}_2$  electrocatalysts with enhanced water oxidation performance. *ACS Catal.* **2017**, *7*, 4214–4220. [[CrossRef](#)]
39. Zhu, C.; Wang, A.L.; Xiao, W.; Chao, D.; Zhang, X.; Tiep, N.H.; Chen, S.; Wang, J.; Kang, X.; Ding, J.; et al. In Situ Grown Epitaxial Heterojunction Exhibits High-Performance Electrocatalytic Water Splitting. *Adv. Mater.* **2018**, *30*, e1705516. [[CrossRef](#)]
40. Chu, L.; Sun, Z.; Cang, L.; Fang, G.; Wang, X.; Zhou, D.; Gao, J. A novel sulfite coupling electro-fenton reactions with ferrous sulfide cathode for anthracene degradation. *Chem. Eng. J.* **2020**, *400*, 125945. [[CrossRef](#)]
41. Xing, M.; Xu, W.; Dong, C.; Bai, Y.; Zeng, J.; Zhou, Y.; Zhang, J.; Yin, Y. Metal sulfides as excellent co-catalysts for  $\text{H}_2\text{O}_2$  decomposition in advanced oxidation processes. *Chem* **2018**, *4*, 1359–1372. [[CrossRef](#)]
42. Zhang, W.; Zhang, Z.; Kwon, S.; Zhang, F.; Stephen, B.; Kim, K.K.; Jung, R.; Kwon, S.; Chung, K.B. Photocatalytic improvement of Mn-adsorbed  $g\text{-C}_3\text{N}_4$ . *Appl. Catal. B* **2017**, *206*, 271–281. [[CrossRef](#)]
43. Sopaj, F.; Oturan, N.; Pinson, J.; Podvorica, F.; Oturan, M.A. Effect of the anode materials on the efficiency of the electro-Fenton process for the mineralization of the antibiotic sulfamethazine. *Appl. Catal. B* **2016**, *199*, 331–341. [[CrossRef](#)]
44. Yang, F.; He, M.; Wu, T.F.; Hao, A.P.; Zhang, S.B.; Chen, Y.D.; Zhou, S.B.; Zhen, L.Y.; Wang, R.; Yuan, Z.L.; et al. Sulfadiazine oxidation by permanganate: Kinetics, mechanistic investigation and toxicity evaluation. *Chem. Eng. J.* **2018**, *349*, 56–65. [[CrossRef](#)]
45. Chen, F.; Yang, F.; Liu, H.; Che, S.; Zhang, G.; Xu, C.; Li, Y. One-pot preparation of surface vulcanization Co-Fe bimetallic aerogel for efficient sulfadiazine degradation. *Chem. Eng. J.* **2022**, *430*, 132–904. [[CrossRef](#)]
46. Wu, Z.; Shen, J.; Ma, N.; Li, Z.; Wu, M.; Xu, D.; Zhang, S.; Feng, W.; Zhu, Y.  $\text{Bi}_4\text{O}_5\text{Br}_2$  nanosheets with vertical aligned facets for efficient visible-light-driven photodegradation of BPA. *Appl. Catal. B* **2021**, *286*, 119–937. [[CrossRef](#)]
47. Deng, F.; Li, S.; Zhou, M.; Zhu, Y.; Qiu, S.; Li, K.; Ma, F.; Jiang, J. A biochar modified nickel-foam cathode with iron-foam catalyst in electro-Fenton for sulfamerazine degradation. *Appl. Catal. B* **2019**, *256*, 117–796. [[CrossRef](#)]
48. Zhang, Y.; Chen, Z.; Wu, P.; Duan, Y.; Zhou, L.; Lai, Y.; Li, S. Three-dimensional heterogeneous Electro-Fenton system with a novel catalytic particle electrode for Bisphenol A removal. *J. Hazard. Mater.* **2020**, *393*, 120448. [[CrossRef](#)]
49. Chen, Y.P.; Yang, L.M.; Chen, J.P.; Zheng, Y.M. Electrospun spongy zero-valent iron as excellent electro-Fenton catalyst for enhanced sulfathiazole removal by a combination of adsorption and electro-catalytic oxidation. *J. Hazard. Mater.* **2019**, *371*, 576–585. [[CrossRef](#)]

50. Liu, K.; Yu, M.; Wang, H.; Wang, J.; Liu, W.; Hoffmann, M. Multiphase Porous Electrochemical Catalysts Derived from Iron-Based Metal-Organic Framework Compounds. *Environ. Sci. Technol.* **2019**, *53*, 6474–6482. [[CrossRef](#)]
51. Xie, W.; Yuan, S.; Mao, X.; Hu, W.; Liao, P.; Tong, M.; Alshwabkeh, A.N. Electrocatalytic activity of Pd-loaded Ti/TiO<sub>2</sub> nanotubes cathode for TCE reduction in groundwater. *Water Res.* **2013**, *47*, 3573–3582. [[CrossRef](#)] [[PubMed](#)]

**Disclaimer/Publisher’s Note:** The statements, opinions and data contained in all publications are solely those of the individual author(s) and contributor(s) and not of MDPI and/or the editor(s). MDPI and/or the editor(s) disclaim responsibility for any injury to people or property resulting from any ideas, methods, instructions or products referred to in the content.